IOP Publishing Smart Materials and Structures
Smart Mater. Struct. 25 (2016) 025008 (14pp) doi:10.1088/0964-1726/25/2/025008

On the effects of geometry, defects, and material asymmetry on the mechanical response of shape memory alloy cellular lattice structures

M R Karamooz Ravari[1,2], S Nasr Esfahani[3], M Taheri Andani[3,4], M Kadkhodaei[1], A Ghaei[1], H Karaca[5] and M Elahinia[3]

[1] Department of Mechanical Engineering, Isfahan University of Technology, Isfahan, 84156-83111, Iran
[2] Department of Mechanical Engineering, Graduate University of Advanced Technology, Kerman 76311-33131, Iran
[3] Dynamic and Smart Systems Laboratory, Mechanical Industrial and Manufacturing Engineering Department, The University of Toledo, OH, 43606, USA
[4] S.M. Wu Manufacturing Research Center, College of Engineering, Department of Mechanical Engineering, University of Michigan, Ann Arbor, MI, 48109, USA
[5] Department of Mechanical Engineering, The University of Kentucky, Lexington, KY, 40506, USA

E-mail: m.karamoozravari@me.iut.ac.ir

Received 29 July 2015, revised 3 November 2015
Accepted for publication 23 November 2015
Published 4 January 2016

Abstract

Shape memory alloy (such as NiTi) cellular lattice structures are a new class of advanced materials with many potential applications. The cost of fabrication of these structures however is high. It is therefore necessary to develop modeling methods to predict the functional behavior of these alloys before fabrication. The main aim of the present study is to assess the effects of geometry, microstructural imperfections and material asymmetric response of dense shape memory alloys on the mechanical response of cellular structures. To this end, several cellular and dense NiTi samples are fabricated using a selective laser melting process. Both cellular and dense specimens were tested in compression in order to obtain their stress–strain response. For modeling purposes, a three -dimensional (3D) constitutive model based on microplane theory which is able to describe the material asymmetry was employed. Five finite element models based on unit cell and multi-cell methods were generated to predict the mechanical response of cellular lattices. The results show the considerable effects of the microstructural imperfections on the mechanical response of the cellular lattice structures. The asymmetric material response of the bulk material also affects the mechanical response of the corresponding cellular structure.

Keywords: shape memory alloys, NiTi, cellular lattice structures, selective laser melting, constitutive model, microplane theory, material asymmetry

(Some figures may appear in colour only in the online journal)

1. Introduction

Cellular materials have potential application in several industrial applications due to their outstanding mechanical properties in combination with low weight. Among these advanced materials, cellular lattice structures (CLSs) are of great importance because their microstructure is regular which allows us to adjust their mechanical properties [1–3]. It is shown that additive manufacturing (AM) methods are promising candidates for fabricating CLSs [4–10]. High cost related to fabrication of CLSs using AM methods makes it necessary to predict their mechanical responses before fabrication. Accordingly, several

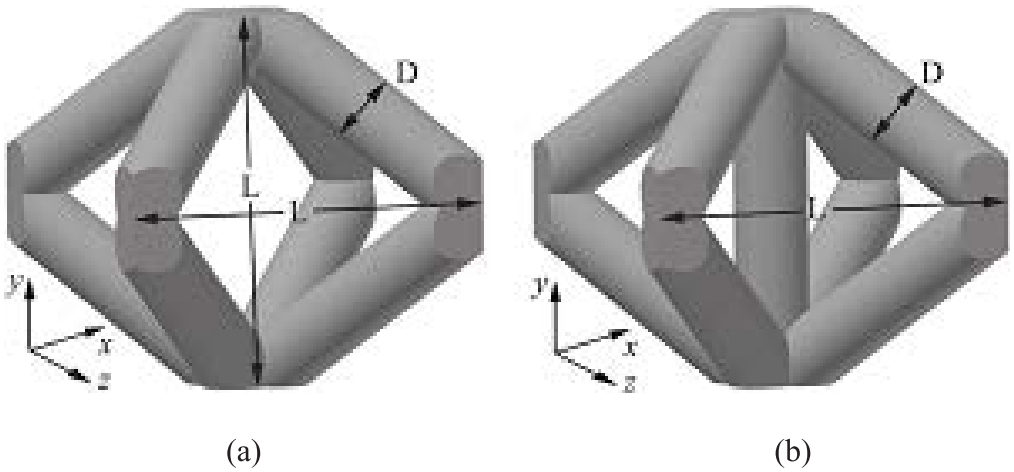

(a) (b)

Figure 1. The repeating unit cell of (a) BCC, (b) BCC-Z cellular lattice structure.

modeling approaches are developed to predict the mechanical response of CLSs. Labeas and Sunaric [11] developed a methodology based on linear static and eigenvalue analysis to study the structural response and failure process of open lattice metallic cellular cores. Ptochos and Labeas [12] used Bernoulli–Euler and Timoshenko beam theories in order to find an analytical solution for elastic moduli and Poisson's ratio of the body-centered cubic (BCC) cellular lattice structures in three Cartesian directions. Gumruk and Mines [13] studied the mechanical compression behavior of 316l stainless steel micro lattices manufactured by selective laser melting (SLM) using theoretical and numerical methods. Smith *et al* [14] used both continuum and beam finite elements to model BCC and BCC-Z architectures under quasi-static compressive loads. Campoli *et al* [15] studied the effects of geometrical irregularities caused by the manufacturing process on the elastic response of CLSs using statistical models. Ushijima *et al* [16] proposed an approach for predicting the yield surface of lattice structures subjected to either a uniaxial or a biaxial stress state utilizing both classical beam theory and finite element technique. Karamooz Ravari *et al* [3] investigated the effect of variations in strut cross-sectional area on the mechanical response of CLSs fabricated by the fused deposition modeling (FDM) method utilizing both beam and continuum finite element approaches. In another work, Karamooz Ravari *et al* [2] proposed a computationally efficient modeling approach to take the microstructural imperfections into account.

Since the fabrication of the first porous shape memory alloys (PSMAs) [17, 18], attempts to fabricate lightweight shape memory alloys (SMAs) have been increased [19–24]. Thanks to additive manufacturing techniques, the production of SMA CLSs with regular microstructural geometry has recently become possible [25, 26]. Although the constitutive modeling of PSMAs is well established in previous studies using micromechanical modeling [27–36] and the finite element method [37–43], analytical and numerical investigations of the mechanical response of SMA CLSs are rarely found in the literature. Machado *et al* [44] created regular cellular materials by joining thin-wall superelastic tubes using electrical resistance welding. They then utilized the finite element approach to simulate the mechanical behavior of these materials. Rahmanian *et al* [45, 46] fabricated CLSs with simple cubic microstructure using the SLM method. They also modeled the CLSs using the unit cell approach and finite element method. However, the fabricated samples could not be considered as infinite repeating of unit cells along periodic vectors and the unit cell method may not yield reliable predictions.

This paper seeks to address the lack of a comprehensive simulation study on the mechanical response of SMA CLSs. To this end, a three-dimensional (3D) constitutive model based on microplane theory, which is capable of taking material asymmetry into account is first introduced. Then, five finite element models, i.e. two models based on the unit cell approach and three models based on the multi-cell method, are generated to simulate the compressive mechanical response of SMA CLSs. Using these models, the effects of microstructural imperfections and asymmetric response of dense SMA on the mechanical response of SMA CLSs are investigated. In order to take the effects of microstructural imperfections into account, a computationally efficient method was successfully implemented for simulation of the mechanical response of SMA CLSs.

2. Material and methods

2.1. Fabrication

Two different types of CLSs including BCC and BCC-Z are investigated in this paper. It is demonstrated that 'angle-ply' lattices, whose struts are oriented at 45°, offer nearly optimized configurations under bending, compression, and shear loadings [2]. These structures are generated by repeating the unit cells shown in figures 1(a) and (b) along x, y, and z directions. As shown in this figure, the BCC unit cell is constructed from eight diagonal struts which connect the center of the upper and lower faces of a cube to the center of its vertical edges. The BCC-Z unit cell has an additional vertical strut which connects the center of the upper and lower faces of the cube.

To comprehensively define the microstructure of the above-mentioned cellular lattices, three different geometrical

Table 1. Process parameters used in SLM machine.

Effective laser power (W)	Layer thickness (μm)	Scanning velocity (m s^{-1})	Hatch distance (μm)	Energy Input (J mm^{-3})
250	30	1.25	120	55.5

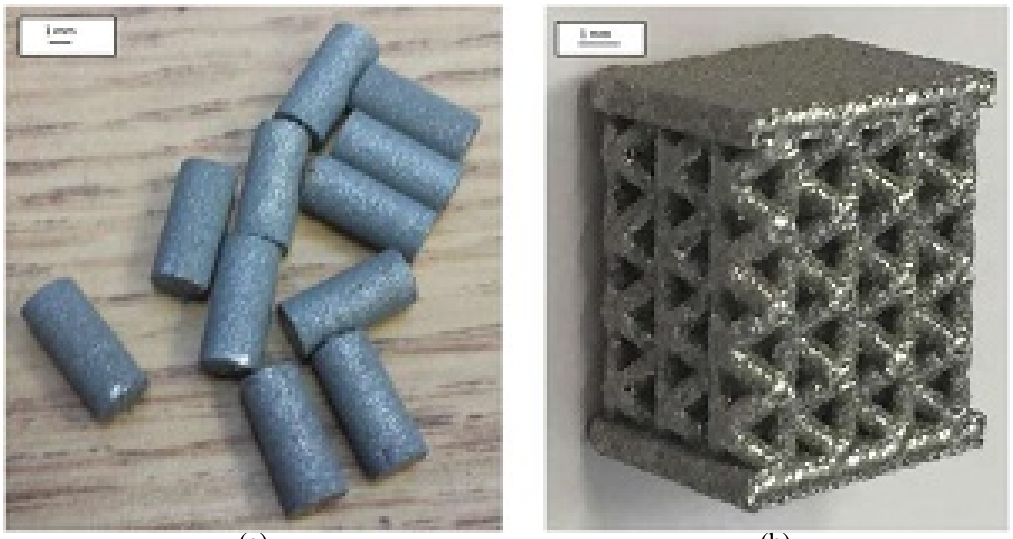

(a) (b)

Figure 2. NiTi (a) bulk samples, (b) BCC cellular lattice structure fabricated by SLM.

parameters should be specified including strut diameter, D, cell length, L, and the number of repeating unit cells along each direction. The level of porosity is defined as the ratio of the pore volumes to the total volume of the dense part. Alternatively, D/L represents the level of porosity. To achieve 69% porosity, the strut diameter and the cell length of both BCC and BCC-Z are assumed to be 0.65 and 2.33 mm, respectively. The samples are constructed by repeating 4, 4, and 3 unit cells along x, y, and z directions, respectively. Note that y is the direction along the height of the sample. In order to be able to carry out compression tests on the CLSs, two plates of 0.933 mm thick are constructed on the upper and lower faces of both the BCC and BCC-Z CLSs.

In this work, a selective laser melting machine made by a PXM Phenix/3D Systems (Rock Hill, SC) is used for fabrication. Ni50.09-Ti (at.-%) ingot (Nitinol Devices & Components, Inc. Fremont, CA) is atomized to powder (25-75 μm particle fractions) by TLS Technik GmbH (Bitterfeld Germany) using the EIGA technique. The process parameters are described in table 1 [47, 48].

Energy input is calculated using the following relation [49]:

$$E = \frac{P}{v.\ h.\ t} \quad (1)$$

where P, v, h, and t are laser power (W), scanning velocity (mm/s), hatch spacing (mm), and layer thickness (mm), respectively.

In order to be able to identify the material parameters of the fabricated dense NiTi for the model, uniaxial compression test samples are fabricated by the same processing parameters as those used for fabrication of cellular lattice structures. Figures 2(a) and (b) show the fabricated bulk and BCC CLS samples, respectively.

2.2. Characterization

Uniaxial compression tests are conducted on the solid and cellular samples. Tests are carried out using a hydraulic Landmark MTS testing machine at the strain rate of 10^{-4} s^{-1}. Heating and cooling rates are fixed at 5 °C min^{-1} and are controlled by a PID-driven Omega temperature controller. Transformation strain is measured by an MTS high-temperature extensometer with a gauge length of 12 mm. In order to make sure that the specimens are in pure martensite phase, samples are first kept in ice water for 2 h and are then exposed to room temperature. All mechanical tests are performed at ambient temperature, i.e. about 23 °C.

Characteristic temperatures for describing the phase transformation are determined by the DSC system (A Perkin–Elmer DSC Pyris 1). Typical temperature range is from −150 to 600 °C, and the heating/cooling rate is 10 K min^{-1}.

Because the parts are produced layer-by-layer in the AM processes, the products always have a few types of defects and imperfections, e.g. variable cross -section along their length, wavy struts, and micro-pores. These defects may change the mechanical properties of CLSs. Figure 3 and figure 4 show SEM images of the microstructure of the BCC and BCCZ NiTi CLSs fabricated by SLM, respectively. Variable cross section can easily be seen along the length of both BCC and BCC-Z structures.

The effects of imperfections should be considered to model the mechanical properties of CLSs. In this work, a cold

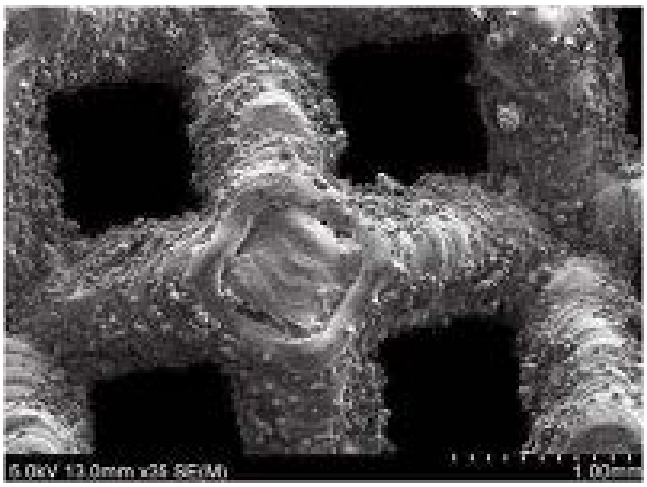

Figure 3. SEM image from BCC structure.

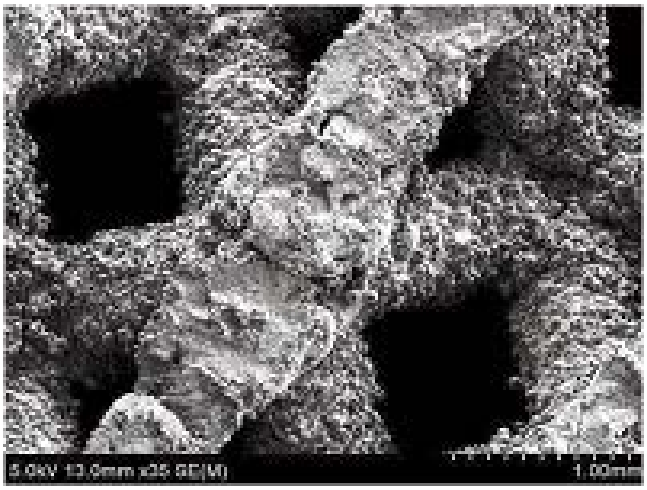

Figure 4. SEM image from BCC-Z structure.

field emission high resolution scanning electron microscope (S-4800) is used to study both structures. The diameters of the struts are measured at several points and the probability of the diameter ranges is determined based on the method proposed by Karamooz Ravari *et al* [3]. Figure 5 shows the probability of the ranges of the strut diameter along the length. This diagram will be used later for constructing the finite element models with microstructural defects.

2.3. SMA constitutive modeling

To simulate the mechanical response of SMA CLSs, a 3D constitutive model is required. In this paper, a 3D constitutive model based on microplane theory considering asymmetric material response is developed. The main idea of this theory is to generalize 1D constitutive relations to 3D ones. According to this theory, the projection of macroscopic stress tensor on each generic microplane is first found. Then, a 1D constitutive relation is defined between micro-level stress and strain. Finally, a homogenization process is used to generalize 1D relations to 3D ones [50–56]. In this section, the above-mentioned three steps are briefly reviewed. For a more

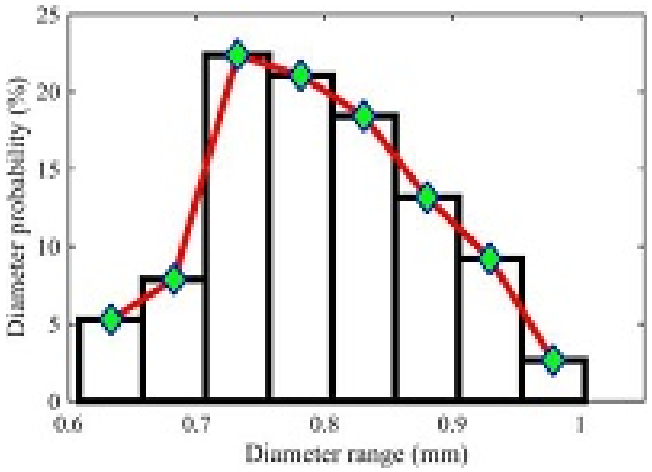

Figure 5. Probability of strut diameter variation along the length.

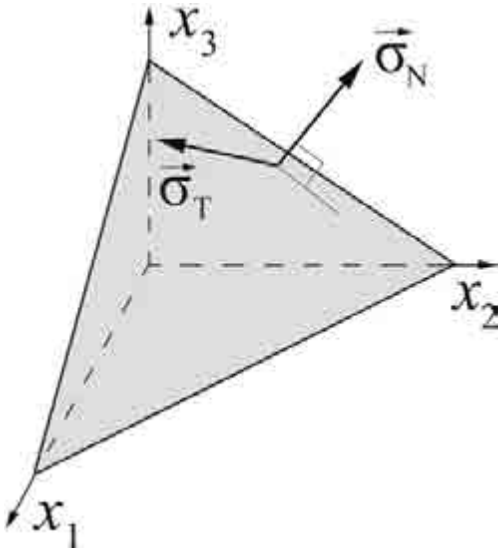

Figure 6. Projection of macroscopic stress tensor on each microplane as normal and shear components.

comprehensive study of this theory, interested readers are referred to [56].

As shown in figure 6, the macroscopic stress tensor can be projected as normal and shear stress vectors on each microplane. These components can be formulated using equation (2) and equation (3) respectively:

$$\sigma_N = N_{ij}\sigma_{ij} \tag{2}$$

$$\sigma_T = T_{ij}\sigma_{ij} \tag{3}$$

In these equations, σ_{ij} is the macroscopic stress tensor, σ_N the normal component, σ_T the shear component, and:

$$N_{ij} = n_i n_j \tag{4}$$

$$T_{ij} = \frac{1}{2}\left(t_i n_j + t_j n_i\right) \tag{5}$$

where n_i are the components of the microplane's unit normal vector and t_i are the components of the unit vector parallel to

the shear stress vector that can be formulated as:

$$t_i = \frac{(\sigma_{ik} n_k - \sigma_N n_i)}{\sqrt{\sigma_{jr}\sigma_{js} n_r n_s - \sigma_N^2}} \tag{6}$$

Previous investigations on the microplane theory showed that if the normal component of projected stress decomposed into volumetric and deviatoric parts, the micro-level elastic modulus is equal to the macroscopic one [50, 51, 56]. Accordingly, this decomposition rule is utilized here as

$$\sigma_N = \sigma_V + \sigma_D \tag{7}$$

in which $\sigma_V = \sigma_{ij}\delta_{ij}/3$ is the volumetric stress, $\sigma_D = (N_{ij} - \delta_{ij}/3)\,\sigma_{ij}$ the deviatoric stress, and δ_{ij} the Kronecker's delta. In microplane theory, it is assumed that the martensitic transformation is associated with the shear stress. So, the volumetric and deviatoric strains can be calculated using Hook's law:

$$\varepsilon_V = \frac{1-2\nu}{E}\sigma_V \tag{8}$$

$$\varepsilon_D = \frac{1+\nu}{E}\sigma_D \tag{9}$$

where ν is the SMAs' Poisson ratio, ε_V the volumetric strain, ε_D the deviatoric strain, and E the elastic modulus of SMA which is defined using the Reuss model [56, 57]:

$$\frac{1}{E} = \frac{1}{E_A} + \xi_s^+\left(\frac{1}{E_M^+} - \frac{1}{E_A}\right) + \xi_s^-\left(\frac{1}{E_M^-} - \frac{1}{E_A}\right) + \xi_T\left(\frac{1}{E_M^T} - \frac{1}{E_A}\right) \tag{10}$$

In this relation, E_A is the austenite elastic modulus, E_M^+ the tensile elastic modulus of stress-induced martensite, E_M^- the compressive elastic modulus of stress-induced martensite, E_M^T the elastic modulus of temperature-induced martensite, ξ_s^+ the stress-induced martensite volume fraction in tension, ξ_s^- the stress-induced martensite volume fraction in compression, and ξ_T the temperature-induced martensite volume fraction. To complete the definition of the 1D micro-level constitutive model, the relation between shear stress, σ_T, and shear strain, ε_T, should be specified. In this regard, the 1D constitutive relation proposed by Poorasadian *et al* [57] is utilized here:

$$\varepsilon_{\mathrm{T}} = \frac{1+\nu}{\mathrm{E}}\sigma_{\mathrm{T}} + \varepsilon_{\mathrm{L}}^+\xi_{\mathrm{s}}^+ + \varepsilon_{\mathrm{L}}^-\xi_{\mathrm{s}}^- \tag{11}$$

in which ε_L is the maximum recoverable strain. The superscripts '+' and '-'respectively denote the tension and compression. To generalize these 1D constitutive relations to 3D ones, the principle of complementary virtual work is used as the homogenization method. This method implies the following relation [50, 51]:

$$\frac{4\pi}{3}\varepsilon_{ij}\sigma_{ij} = 2\int_\Omega \left(\varepsilon_V\,\delta\sigma_V + \varepsilon_D\,\delta\sigma_D + \varepsilon_T\,\delta\sigma_T\right)d\Omega \tag{12}$$

where Ω is the surface of a unit hemisphere, and ε_{ij} the macroscopic strain tensor. Substitution of equations (2), (3), (7), (8), (9), and (11) into equation (12) followed by simplifications leads to the following relation between macroscopic stress and strain tensors [56]:

$$\varepsilon_{ij} = -\frac{\nu}{E}\sigma_{mm}\delta_{ij} + \frac{1+\nu}{E}\sigma_{mn}\cdot\frac{3}{2\pi} \times \int_\Omega \left(N_{mn}N_{ij} + T_{mn}T_{ij}\right)d\Omega + \left(\varepsilon_L^+\xi_s^+ + \varepsilon_L^-\xi_s^-\right)\cdot\frac{3}{2\pi}\int^\Omega T_{ij}\,d\Omega \tag{13}$$

To finalize the constitutive model, the evolution of martensitic volume fractions must be specified. Referring to figure 7, evolution of stress-induced as well as temperature-induced martensite volume fraction can be calculated as a function of equivalent stress and temperature at each material point using the following relations [56]:

$$\begin{cases} \textit{if } T \leqslant M_s \textit{ and } \sigma_s^{cr} < \hat{\sigma} < \sigma_f^{cr}: \\ \quad Y = \cos\left(\dfrac{\pi}{\sigma_f^{cr} - \sigma_s^{cr}}\left(\hat{\sigma} - \sigma_s^{cr}\right)\right) \\ \quad \xi_S^r = \dfrac{1-Y}{2} + \xi_{S0}^r = \dfrac{1-Y}{2}, \\ \quad \xi_S^p = \xi_{S0}^p\dfrac{1-\xi_S^r}{1-\xi_{S0}^r},\ \xi_T = \left(\xi_{T0} + \Delta\right)\dfrac{\left(1-\xi_S^r\right)}{1-\xi_{S0}^r} \\ \quad \textit{if } T < M_f\text{: } \Delta = 0 \\ \quad \textit{else: } \Delta = \dfrac{1-\xi_0}{2}\left(1 - Y_{MT}\right) \\ \textit{if } T > M_s \textit{ and } \sigma_s^{cr} + C_M\left(T - M_s\right) \\ \quad < \hat{\sigma} < \sigma_f^{cr} + C_M\left(T - M_s\right): \\ \quad Y = \cos\left(\dfrac{\pi}{\sigma_f^{cr} - \sigma_s^{cr}}\left(\hat{\sigma} - \sigma_s^{cr}\right.\right. \\ \quad \left.\left. - C_M\left(T - M_s\right)\right)\right) \\ \quad \xi_S^r = \dfrac{1-Y}{2} + \xi_{S0}^r\dfrac{1+Y}{2}, \quad \xi_S^p \\ \quad = \xi_{S0}^p\dfrac{1-\xi_S^r}{1-\xi_{S0}^p},\ \xi_T = \xi_{T0}\dfrac{1-\xi_S^r}{1-\xi_{S0}^p} \\ \textit{if } T > A_s \textit{ and } C_{Af}\left(T - A_f\right) \\ \quad < \hat{\sigma} < C_{AS}\left(T - A_s\right): \\ \quad Y = \cos\left(\dfrac{\pi}{C_{As}\left(T - A_s\right) - C_{Af}\left(T - A_f\right)}\right. \\ \quad \left.\times\left(C_{AS}\left(T - A_s\right) - \hat{\sigma}\right)\right) \\ \quad \xi_S^r = \dfrac{\xi_{S0}^r}{2}(1+Y),\ \xi_S^P = \dfrac{\xi_{S0}^r}{2}(1+Y), \\ \quad \xi_T = \dfrac{\xi_{T0}}{2}(1+Y) \\ \textit{if } M_f < T < M_s \textit{ and } \hat{\sigma} < \sigma_s^{Cr} \\ \quad \xi_S^r = \xi_{S0}^r, \quad \xi_S^P = \xi_{S0}^r, \quad \xi_T \\ \quad = \dfrac{1-\xi_0}{2}\left(1 - Y_{MT}\right) + \xi_{T0} \end{cases} \tag{14}$$

Table 2. Description of the presented models.

Model Name	Description
UC	Unit cell model + stress–strain response of the dense SMA as the bulk material
UC + SS	Unit cell model + stress–strain response of the single defected strut as the bulk material
MC	Multi-cell model without defect + stress–strain response of the dense SMA as the bulk material
MC + SS	Multi-cell model without defect + stress–strain response of the single defected strut as the bulk material
MCD	Multi-cell model with defect + stress–strain response of the dense SMA as the bulk material

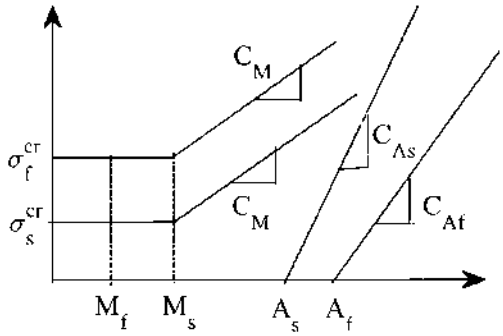

Figure 7. The stress–temperature phase diagram of SMA.

In this relation, 'r' and 'p' are '+' and '−' in tensile loading and '−' and '+' in the compressive one. $\hat{\sigma}$ is the equivalent stress which is based on the second and third invariants of macroscopic deviatoric stress tensor, J_2 and J_3, to account for material asymmetry [56]:

$$\hat{\sigma} = \frac{1}{1+\beta}\left\{\sqrt{3J_2} + \frac{9}{2}\beta\frac{J_3}{J_2}\right\} \tag{15}$$

2.4. Finite element modeling of cellular lattice structures

In this subsection, five finite element models are developed to predict the mechanical stress–strain response of SMA CLSs. Two models are based on the unit cell approach while three models are based on the multi-cell method. These models are described in the subsections below. Table 2 summarizes the models and their brief description.

2.4.1. Unit cell model without defect (UC). Figures 8(a) and (b) show the meshed unit cell model utilized for the modeling of BCC and BCC-Z CLSs, respectively. Since the unit cell model is used, the periodic boundary conditions should be applied for modeling purposes. In order to do so, suppose that the utilized unit cell has three opposite pairs of surfaces as $(\partial R_{i1},\ \partial R_{i2})$, i = 1, 2, 3. The following constraints should be applied between the degrees of freedom, **u**, of the paired faces:

$$u_{i1} - u_{i2} = u_{i1}^{ref} - u_{i2}^{ref}, \qquad i = 1,\ 2,\ 3 \tag{16}$$

where the superscript 'ref' denotes reference points on the paired faces. After applying the boundary conditions, the upper face of the unit cell is compressed with the value of Δ for displacement.

2.4.2. Unit cell model with defect. Karamooz Ravari *et al* [3] showed that microstructural defects can considerably affect the mechanical response of CLSs. To account for these intrinsic imperfections in the unit cell model, the method proposed by Karamooz Ravari and Kadkhodaei [2] is used here. They presented a computationally efficient modeling approach based on the experimental observations reported by Tsopanos *et al* [9] and Gumrum and Mines [13]. In this method, a single strut of CLSs, consisting of strut's cross-sectional variation along its length and deviation from straightness, is modeled under uniaxial tension (compression) and its stress–strain response is found. Then, the material parameters related to this curve are attributed to the bulk material of the unit cell model without any defect. This model is abbreviated as 'SS' in the rest of this paper. The combination of this method with other strategies is accompanied by '+SS' e.g. 'UC + SS' stands for the combination of a unit cell model with a single strut one. Here, this modeling approach is briefly explained:

To construct the strut's geometry, it is assumed that each strut is formed as layers of spherical elements. Referring to figure 9, the amount of penetration for two neighboring spheres, with radii R_1 and R_2, is L_p.

In addition, the maximum deviation positioned in the center of spheres from the strut axis, i.e. deviation from straightness in a wavy strut, is assumed to be A_d. To model these defects, the centerline of the strut is first generated. Then, some spheres with random diameters are generated along this line until the strut's length, L_s, reaches the desired value. To determine the spheres' diameters, the method provided in [3] is utilized in this paper. In this method, an index is assigned to the strut diameter's intervals of the probability diagram depicted in figure 5. Then, a set of indices is generated in which each index is repeated M times, where M is the nearest integer number to the probability of that diameter range. To choose a value for the sphere diameter, an integer number between 1 and 100 is generated randomly and the corresponding diameter range is selected. Then, a random number is produced in this range using the following equation:

$$D = D_{\min} + r \times \left(D_{\max} - D_{\min}\right) \tag{17}$$

where r is a random number between 0 and 1, and D_{min} and $D_{\max}$ are respectively the minimum and maximum values of the struts' diameters in the diameter range denoted by the chosen index. To model the wavy strut defects, the center of each sphere is shifted to a random position, A_d, using

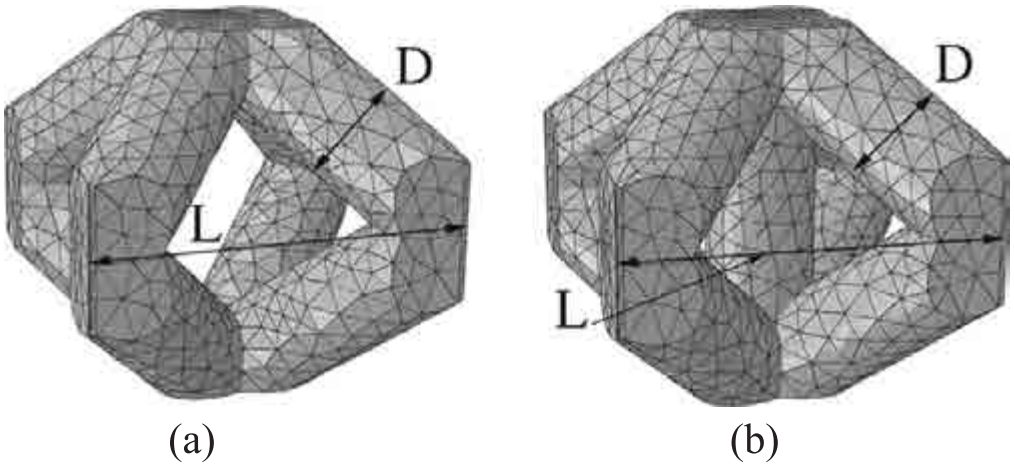

Figure 8. The meshed configuration of (a) BCC (b) BCC-Z unit cell model.

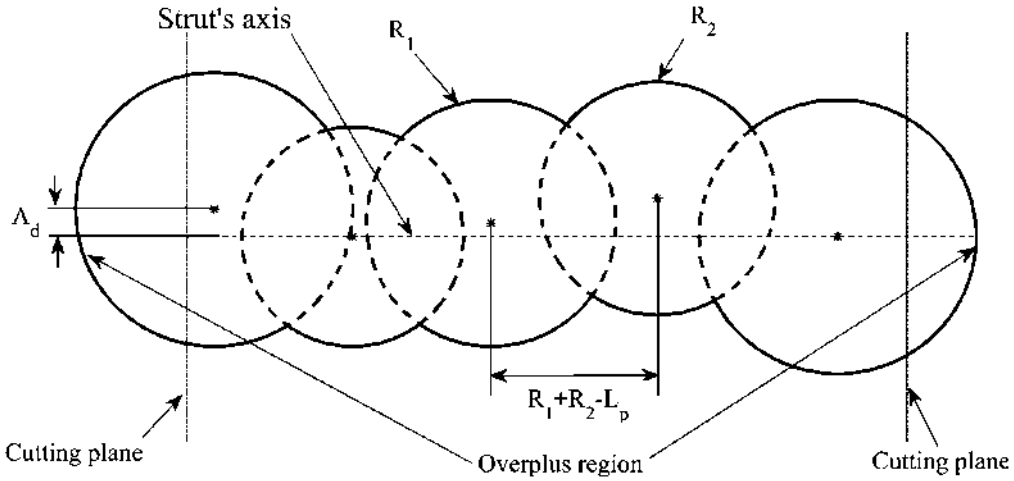

Figure 9. Two-dimensional (2D) schematic representation of single strut model.

equation (18):

$$A_d = r \times A_d^{\max} \tag{18}$$

in which $A_d^{\max}$ is the maximum value of deviation from straightness and is obtained using SEM images. After satisfying the strut's length, the overplus regions are removed using two cutting planes. Figure 10 shows the 3D representation of the single strut model which is obtained using the SEM data.

After generating the geometry of the single strut, all degrees of freedom at one end of the strut are fixed and the other end is stretched (compressed) and the stress–strain response is calculated using the following relations:

$$\sigma = \frac{4F}{\pi D_{av}^2} \tag{19}$$

$$\varepsilon = \frac{\delta}{L_s} \tag{20}$$

where δ is the applied displacement, D_{av} the average value of the strut's diameter, and F the reaction force.

Figure 10. 3D representation of the strut model produced using the SEM data.

2.4.3. Multi-cell model without defect. Since in the unit cell model a cellular material is supposed to be an infinite medium, this model can present reliable results only when the cell size is small enough compared to the sample size [58]. In the present study, however, the cellular samples consist of only 48 unit cells and the unit cell method may cause over-prediction of the stress level at a specific strain value. To assess this issue, a multi-cell model (MC) representing the

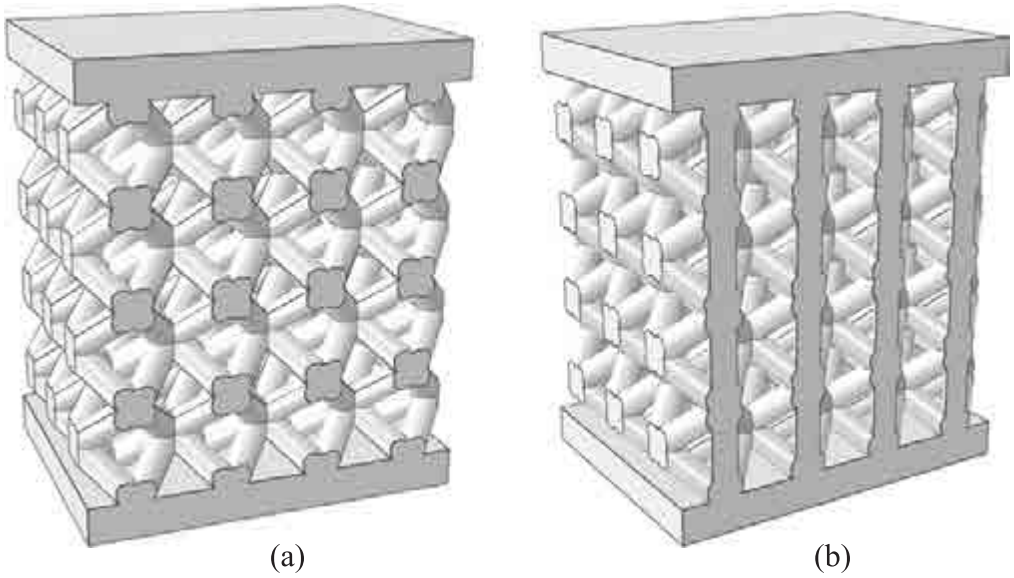

Figure 11. Multi-cell model without defect for (a) BCC (b) BCC-Z cellular lattice structures.

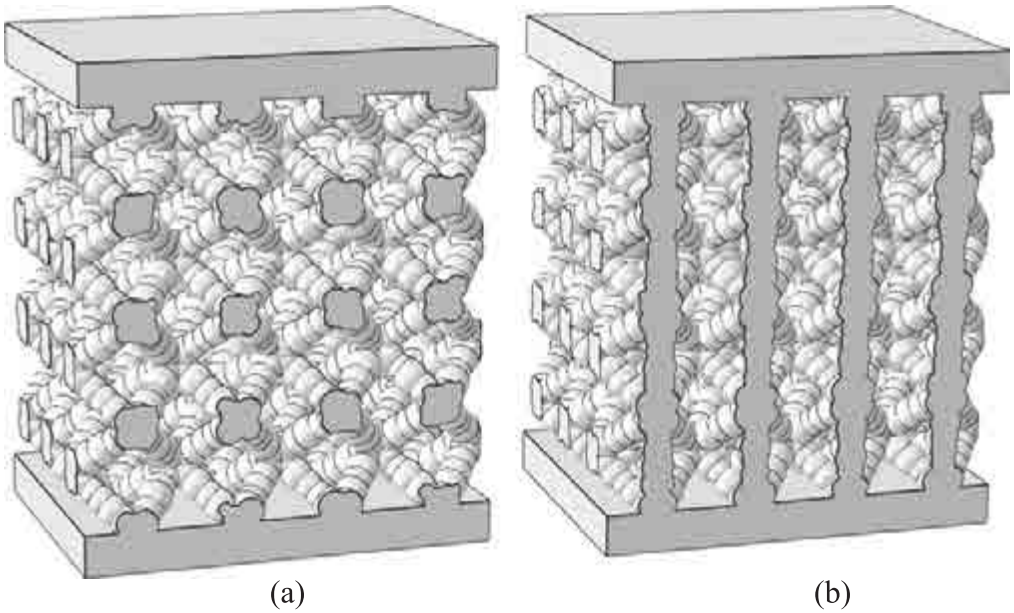

Figure 12. MCD model for (a) BCC (b) BCC-Z cellular lattice structure.

real utilized sample is also modeled. A python script is developed as the input of the ABAQUS finite element package to generate both BCC and BCC-Z CLSs. Two plates of 0.933 mm thick are constructed at the top and bottom of the models to match with measurements in the experiments. Figures 11(a) and (b) show the MC models for BCC and BCC-Z CLSs, respectively.

2.4.4. Multi-cell model with defects. To include the microstructural defects in the MC model, two approaches are employed here. In the first approach, the stress–strain response of the SS model, presented in subsection 2-4-2, is used as the bulk material of the MC model presented in the previous subsection. In another approach, all the ligaments of the MC model are generated in a manner analogous to the one for single strut. Consequently, all the struts of the model have variations in their diameter as well as deviation from straightness in their microstructure. Figures 12(a) and (b) show the proposed MC model for BCC and BCC-Z CLSs, respectively. This model is denoted by MCD in the rest of this paper.

3. Results and discussion

In this section, the results of the above-mentioned modeling approaches are presented and compared with the experiment. Moreover, predictions of different proposed approaches are

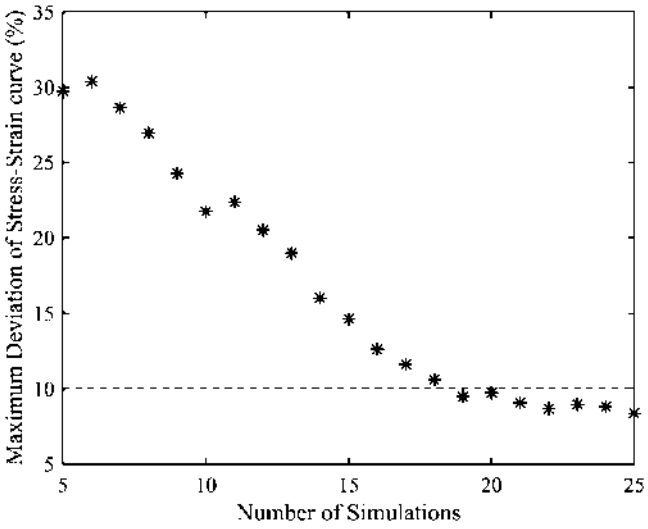

Figure 13. Variation of the maximum deviation in stress–strain curves with the number of simulations.

compared with each other. It is worth mentioning that, for the models with random microstructure, the results may be different from run to run. In order to reduce the effects of randomness in the simulations, each simulation is repeated until the maximum variations in the stress–strain responses gets smaller than 10%. As shown in figure 13, the maximum value of deviation is about 10% after 19 simulations. Accordingly, each simulation was repeated 20 times and the average stress–strain response is reported. Note that the maximum deviation is related to the point at which the maximum stress is applied. The models are meshed using 10-node modified quadratic tetrahedron elements denoted by C3D10M in ABAQUS. A mesh sensitivity analysis is performed for each model in such a way that the mesh size is reduced until changes in the obtained stress–strain response are negligible. After the mesh convergence study, the mesh size is obtained to be 0.025, 0.2, 0.2, and 0.025 for SS, UC, MC, and MCD models, respectively. All the simulations are performed on 2 Intel Xeon X5670 (12 core), 2.93 GHz processors with 24 cores and 20 GB RAM.

3.1. Experimental results

In order to identify the material parameters for the bulk SMA, the transformation temperatures first need to be determined. In this regard, the DSC test described in sections 2–1 is performed and the corresponding diagram is presented in figure 14. Using this diagram, the transformation temperatures are determined as follows: $M_f = 26\,^{\circ}\mathrm{C}$, $M_s = 54.1\,^{\circ}\mathrm{C}$, $A_s = 59\,^{\circ}\mathrm{C}$, and $A_f = 84.5\,^{\circ}\mathrm{C}$.

In order to determine the maximum allowable applied stress before experiencing large plastic deformations on both dense SMA and SMA CLSs, both dense and CLS specimens are first loaded in compression until fracture as shown in figures 15(a) and (b). Using these figures, the maximum stress level for loading–unloading tests is determined to be 802, 50, and 90 MPa for dense SMA, BCC CLSs, and BCC-Z CLSs, respectively.

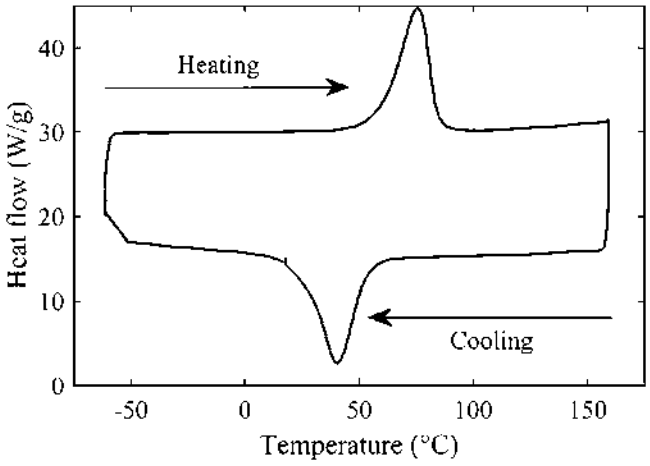

Figure 14. DSC test on an SLM-fabricated dense part.

Figures 16(a) and 15(b) show stress–strain response in a loading–unloading cycle for dense and CLSs respectively. As shown in figures 17 and 18, after unloading, all the specimens are heated up to 150 °C which is above the austenite finish temperature. Then, the samples are cooled down to about −50 °C and again heated up to the ambient temperature.

3.2. Calibration of material parameters

The material parameters are obtained using the experimental compressive stress–strain response of the bulk sample as well as DSC measurements. In this regard, the slope of the stress–strain curve of dense SMA at the unloading portion is reported as the martensite elastic modulus, and the unrecovered strain at the end of the unloading, before heating the sample, is considered as the maximum recoverable strain. Then, the values of σ_s^{cr} and σ_f^{cr} are assessed according to the experimental stress–strain curve. Table 3 shows the obtained material parameters. To assess the effects of material asymmetry on the mechanical stress–strain response of CLSs, the symmetric material behavior of the dense SMA is first considered by setting $\beta = 0$. Then, the effects of material asymmetry on the mechanical behavior of the CLSs are investigated. Since all the experimental measurements and finite element simulations are performed at $T = 23\,^{\circ}\mathrm{C}$, which is below the martensite start temperature, only the presented material parameters in this table are necessary and the others are optional.

3.3. Single strut model

Figure 19 compares the stress–strain curve of the SS model with the experimental response of the bulk material. It can be clearly seen from this curve that, at the same magnitude of strain, the stress level is lower for the SS model than the bulk material. This is due to the existence of two kinds of imperfections in the SS model: strut diameter variation along its length and deviation from straightness.

To be able to use the stress–strain response of the SS as the bulk material of the UC as well as the MC model, it is necessary to obtain the material parameters related to the

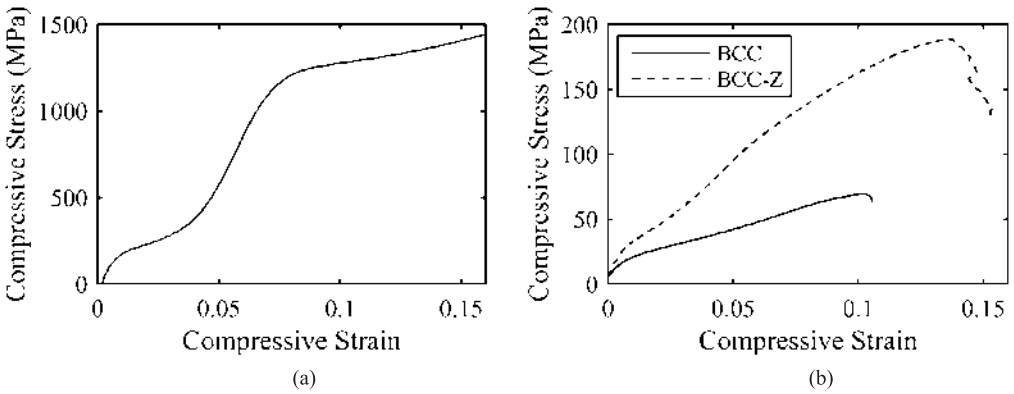

Figure 15. Stress–strain response of (a) dense SMA (b) SMA CLSs until fracture.

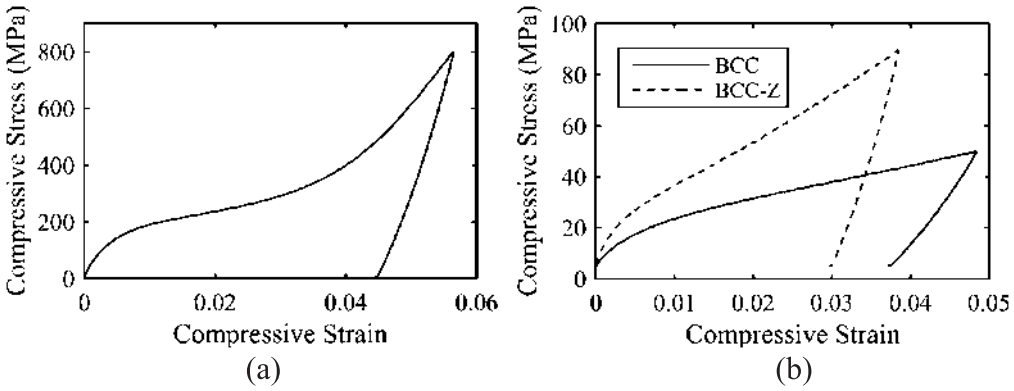

Figure 16. The loading–unloading cycle of stress–strain response for (a) dense, (b) CLSs.

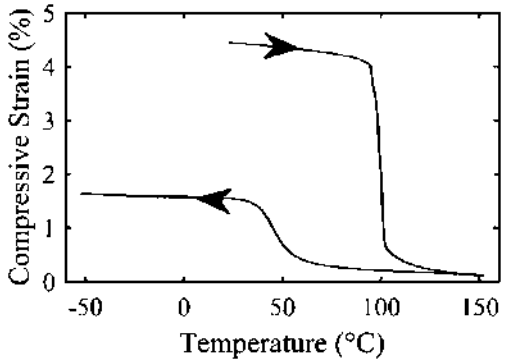

Figure 17. Change in compressive strain with temperature for dense SMA.

stress–strain response of the SS model. Table 4 shows these material parameters which are obtained using the stress–strain response of SS shown in figure 19.

3.4. Cellular lattice structures modeling

Figure 20 shows the stress–strain response of BCC and BCC-Z cellular lattice structures, respectively. In these figures, the results of the UC, UC + SS, MC, MC + SS, and MCD models are compared with experimental findings. It is obvious from these curves that both models based on the unit cell model significantly over-predict the stress level. As stated earlier, it is because the unit cell size is not small enough in comparison with the fabricated specimens indicating that the unit cell model is not a good candidate for modeling purposes.

By comparing the MC models, it can be concluded that the existence of defects in the struts of CLSs can significantly affect their mechanical responses. As can be seen, the MC model has the highest stress level while the MCD model has the lowest one. The maximum error relative to the experimental results is about 53% for MC, 35% for MC+SS, and 22.7% for the MCD model in the case of BCC CLS. These values are respectively 43.8, 19.3, and 12.1% for BCC-Z CLS. The reason the stress level of the MC+SS model is higher than that of MCD is that the latter has more defects in its microstructure. In addition, the defective struts experience bending, shearing, and axial loads in the MCD model while the defective single strut response is obtained only under axial loading. It is worth mentioning that the computational cost of the MCD model is almost eight times higher than that for MC+SS. Therefore, one may condone the greater error of the latter for more computational efficiency.

3.5. Effects of SMA material asymmetry response

It is previously reported that the transformation surface of a dense SMA is not symmetric [43, 59]. This inherent behavior causes the tension–compression asymmetry of the dense SMAs. To assess the effects of this asymmetric response on the mechanical stress–strain response of the SMA CLSs, two

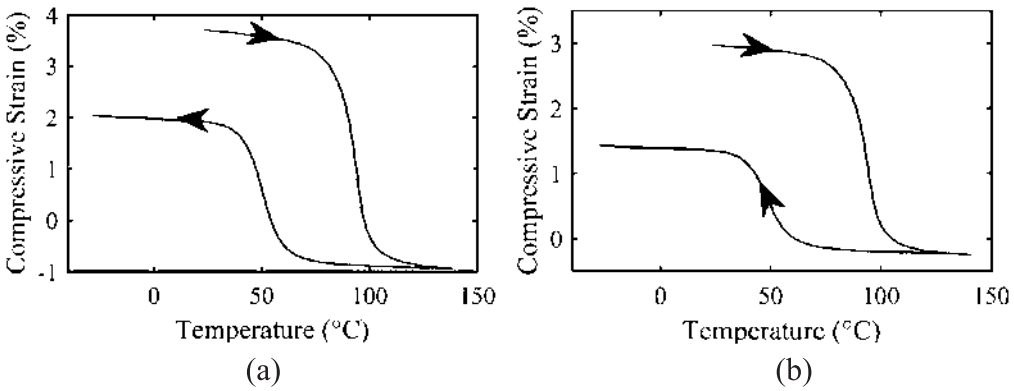

Figure 18. Change in compressive strain with temperature for (a) BCC (b) BCC-Z CLSs.

Table 3. Material parameters of bulk material utilized for the simulations in the symmetric model.

ν	E_M (MPa)	σ_s^{cr} (MPa)	σ_f^{cr} (MPa)	ε_L	M_f (°C)	M_f (°C)	A_s (°C)	A_f (°C)
0.3	69 000	85	450	0.045	26	54.1	59	84.5

Table 4. Material parameters obtained using the stress–strain response of the single strut model.

ν	E_M (MPa)	σ_s^{cr} (MPa)	σ_f^{cr} (MPa)	ε_L	M_f (°C)	M_f (°C)	A_s (°C)	A_f (°C)
0.3	51 000	38	438	0.043	26	54.1	59	84.5

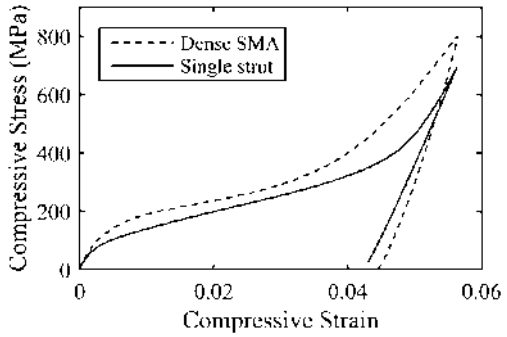

Figure 19. Comparison of the stress–strain response of single strut model and experimental one of bulk SMA.

strategies are employed in this paper. In the first strategy, denoted by MCD + AM, the model considering material asymmetry is used as the constitutive model for the simulation of the MCD model. Table 5 shows the material parameters used for this simulation. In this table, the material parameters obtained in the previous section are considered for the compressive response, and those related to tension are obtained based on what is commonly reported for polycrystalline NiTi. That is, the elastic modulus of the martensite phase in compression is supposed to be greater than that in tension. In addition, the maximum recoverable strain in tension is assumed to be about twice that of compression. The value of the asymmetry level is considered to be about 0.16 as reported by Lubliner and Auricchio [60].

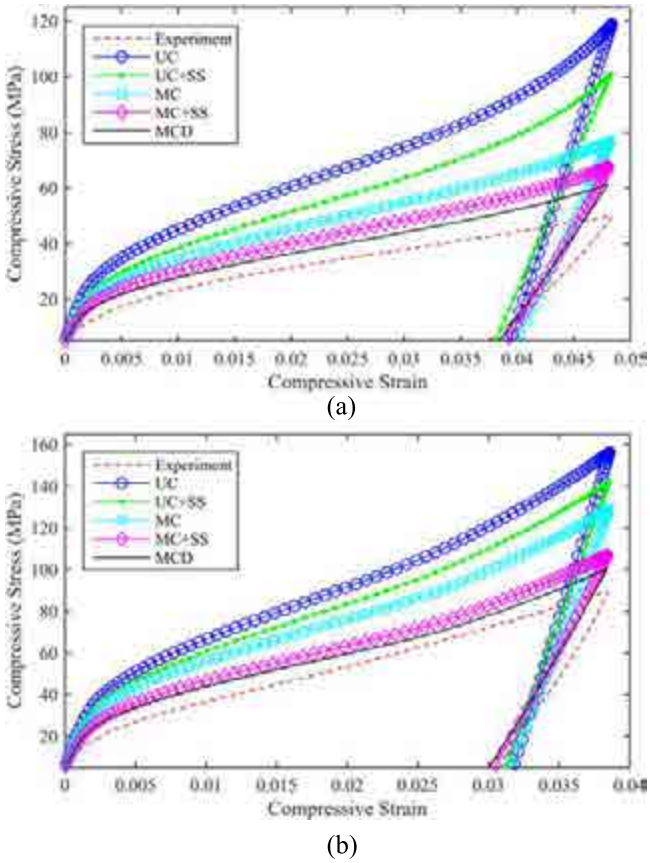

Figure 20. Comparison of the numerical and empirical stress–strain responses for (a) BCC and (b) BCC-Z cellular lattice structures.

Table 5. Material parameters utilized for investigation of the asymmetric response.

E_M^+ (*MPa*)	E_M^- (*MPa*)	ν	σ_s^{cr} (*MPa*)	σ_f^{cr} (*MPa*)	ε_L^+	ε_L^-	β
50 000	69 000	0.3	61.55	325.9	0.07	−0.045	325.9

Table 6. Material parameters obtained using the tensile and compressive stress–strain response of the single strut.

E_M^+ (*MPa*)	E_M^- (*MPa*)	ν	σ_s^{cr} (*MPa*)	σ_f^{cr} (*MPa*)	ε_L^+	ε_L^-	β
36 950	51 000	0.3	27.51	317.2	0.062	−0.042	0.16

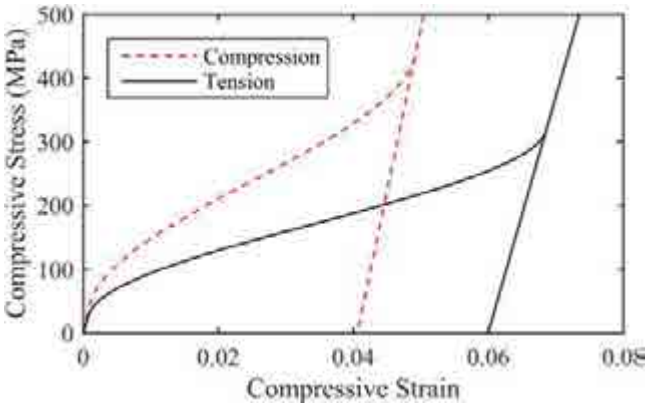

Figure 21. Stress–strain response of NiTi single strut in tension and compression.

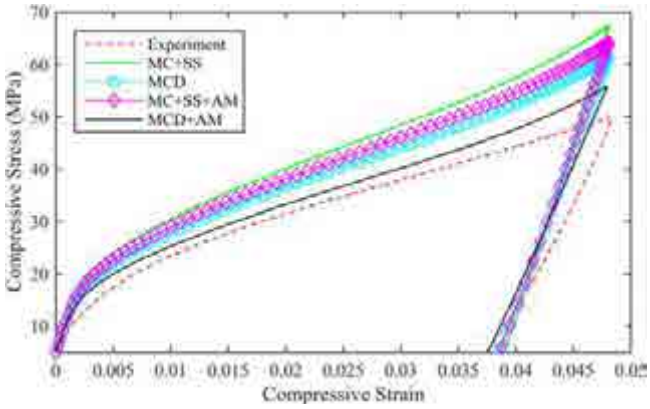

Figure 22. Comparison of the stress–strain response of the BCC cellular lattice structure obtained using MC + SS, MCD, MC + SS + AM, and MCD + AM with the experimental one.

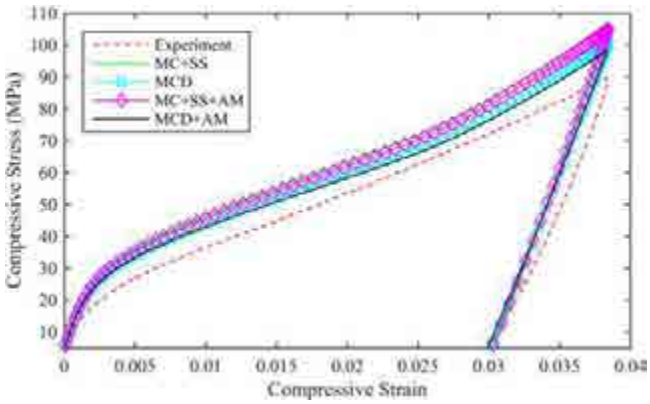

Figure 23. Comparison of the stress–strain response of the BCC-Z cellular lattice structure obtained using MC + SS, MCD, MC + SS + AM, and MCD + AM with the experimental one.

In the second strategy, denoted as the MC + SS + AM model, the single strut is modeled using the asymmetric constitutive model, and its tensile as well as compressive stress–strain response is obtained (figure 21). Then, the material parameters related to these stress–strain responses are obtained and attributed to the bulk material of the MC model. Table 6 shows the material parameters obtained using the stress–strain response of the single strut in tension and compression.

Figure 22 compares the stress–strain response of the BCC CLS obtained using MC + SS, MCD, MC + SS + AM, and MCD + AM with the empirical curve. As seen from this curve, the material asymmetry affects the stress–strain response of the BCC CLS and reduces the stress level. In addition, the predictions of the asymmetric model are in better agreement with the experimental stress–strain response. In this case, the maximum error relative to the experiment reduces to 28.3 and 11.7% for MC + SS + AM and MCD + AM models, respectively.

Referring to figure 23, unlike the BCC CLS, introducing the material asymmetric response does not affect the stress–strain response of the BCC-Z CLS because the dominant deformation mechanism in the BCC-Z CLS is axial loading due to the existence of the vertical strut. However, the dominant deformation mechanism in the BCC CLS is bending which submits some regions of the ligaments to tension and some other regions to compression. In this case, maximum error relative to the experimental stress–strain curve is about 17 and 9.9% for MC + SS + AM and MCD + AM models, respectively. It shows that introducing the asymmetric material response into the modeling of BCC-Z CLS decreases the relative error about 2%. This improvement is about 8% in the case of the BCC cellular lattice.

4. Conclusion

This paper deals with the simulation of SMA CLSs using the finite element method. The main aim was to investigate the

effects of both microstructural imperfections and the asymmetric response of dense SMA on the mechanical response of SMA CLSs. Therefore, a constitutive model was combined with five different finite element models with and without microstructural imperfections. The obtained results showed that the unit cell model was not suitable to study the mechanical response of these CLSs because the fabricated CLSs could not be considered as an infinite periodic lattice. It was also observed that the microstructural imperfections significantly affected the effective response of SMA CLSs. Since considering the microstructural imperfections increased the computational time, a computationally efficient method was utilized to overcome this difficulty. The results showed that, by compromising about ten percent error, the computationally efficient method could be used for taking microstructural imperfections into account. Finally, the effects of the material asymmetric response of dense SMA on the mechanical response of SMA CLSs were assessed by comparing the mechanical response of CLSs obtained by symmetric and asymmetric constitutive models. The results demonstrated that as the portion of the axial load in the deformation mechanisms of SMA CLSs increased, the effects of the material asymmetric response of dense SMA decreased.

Acknowledgments

All the simulations were run at the National High-Performance Computing Center of Isfahan University of Technology. The authors would like to thank Dr Ashrafizadeh for providing us with access to the facilities of this center.

References

[1] Karamooz Ravari M and Kadkhodaei M 2013 Presented at the Poromechanics V *Proc. Fifth Biot Conf. on Poromechanics (Vienna, Austria)* 1021–8
[2] Karamooz Ravari M and Kadkhodaei M 2015 *J. Mater. Eng. Perform.* **24** 245–52
[3] Karamooz Ravari M R, Kadkhodaei M, Badrossamay M and Rezaei R 2014 *Int. J. Mech. Sci.* **88** 154–61
[4] Yang L 2015 *Rapid Prototyping J.* **21** 168–76
[5] Yavari S A, Ahmadi S M, Wauthle R, Pouran B, Schrooten J, Weinans H and Zadpoor A A 2015 *J. Mech. Behav. Biomed. Mater.* **43** 91–100
[6] Santorinaios M, Brooks W, Sutcliffe C J and Mines R A W 2006 *WIT Transactions on The Built Environment* **85** 481–90
[7] Mines R A W 2008 *Strain* **44** 71–83
[8] McKown S, Shen Y, Brookes W K, Sutcliffe C J, Cantwell W J, Langdon G S, Nurick G N and Theobald M D 2008 *Int. J. Impact Eng.* **35** 795–810
[9] Tsopanos S, Mines R A W, McKown S, Shen Y, Cantwell W J, Brooks W and Sutcliffe C J 2010 *J. of Manufacturing Science and Engineering* **132** 041011
[10] Yan C, Hao L, Hussein A and Raymont D 2012 *International J. of Machine Tools and Manufacture* **62** 32–8
[11] Labeas G N and Sunaric M M 2010 *Strain* **46** 195–204
[12] Ptochos E and Labeas G 2012 *J. Sandwich Structures and Materials* **14** 597–626
[13] Gumruk R and Mines R A W 2013 *Int. J. Mech. Sci.* **68** 125–39
[14] Smith M, Guan Z and Cantwell W 2013 *Int. J. Mech. Sci.* **67** 28–41
[15] Campoli G, Borleffs M S, Amin Yavari S, Wauthle R, Weinans H and Zadpoor A A 2013 *Mater. Des.* **49** 957–65
[16] Ushijima K, Cantwell W and Chen D 2013 *Int. J. Mech. Sci.* **68** 47–55
[17] Martynova I, Skorohod V, Solonin S and Goncharuk S 1991 *J. Phys. IV* **1** C421–C424
[18] Itin V I, Gjunter V E, Shabaloyskaya S A and Sacheva R L C 1994 *Mater. Character.* **32** 179–87
[19] Shishkovsky I, Yadroitsev I and Smurov I 2012 *Physics Procedia* **39** 447–54
[20] Shishkovskii I V, Morozov Y G, Fokeev S V and Volova L T 2012 *Powder Metall. Met. Ceram.* **50** 606–18
[21] Shishkovsky I 2012 *Physics Procedia* **39** 893–902
[22] Shishkovsky I 2005 *Technical Physics Letters* **31** 186–8
[23] Elahinia M H, Hashemi M, Tabesh M and Bhaduri S B 2012 *Prog. Mater. Sci.* **57** 911–46
[24] Habijan T, Haberland C, Meier H, Frenzel J, Wittsiepe J, Wuwer C, Greulich C, Schildhauer T and Köller M 2013 *Materials Science and Engineering:* C **33** 419–26
[25] Andani M T, Moghaddam N S, Haberland C, Dean D, Miller M J and Elahinia M 2014 *Acta Biomaterialia* **10** 4058–70
[26] Walker J, Andani M T, Haberland C and Elahinia M 2014 *ASME 2014 International Mechanical Engineering Congress and Exposition* vol 2A paper no IMECE2014-40432
[27] Entechev P B and Lagoudas D C 2002 *Mech. Mater.* **34** 1–24
[28] Entchev P B and Lagoudas D C 2004 *Mech. Mater.* **36** 893–913
[29] Zhao Y, Taya M, Kang Y and Kawasaki A 2005 *Acta Mater.* **53** 337–43
[30] Nemat-Nasser S, Su Y, Guo W-G and Isaacs J 2005 *J. Mech. Phys. Solids* **53** 2320–46
[31] Zhao Y and Taya M 2007 *J. Applied Mechanics* **74** 291
[32] Toi Y and Choi D 2008 *J. Computational Science and Technology* **2** 511–22
[33] Liu B, Dui G, Zhu Y, Selvadurai A, Selvadurai P, Liu A C-M, Yang C-C, Huang S-Y, Chen W-H and Wu C-H 2010 *Structural Longevity* **4** 113–20
[34] Zhu Y and Dui G 2011 *Acta Mech. Solida Sin.* **24** 289–97
[35] Olsen J S and Zhang Z L 2012 *Int. J. Solids Struct.* **49** 1947–60
[36] Liu B, Dui G, Xie B and Xue L 2014 *J. Mech. Behav. Biomed. Mater.* **32** 185–91
[37] Qidwai M A, Entchev P B, Lagoudas D C and DeGiorgi V G 2001 *Int. J. Solids Struct.* **38** 8653–71
[38] DeGiorgi V G and Qidwai M A 2002 *Smart Mater. Struct.* **11** 435–43
[39] Panico M and Brinson L C 2008 *Int. J. Solids Struct.* **45** 5613–26
[40] Sayed T E, Gürses E and Siddiq A 2012 *Comput. Mater. Sci.* **60** 44–52
[41] Liu B, Dui G and Zhu Y 2012 *J. Mech. Behav. Biomed. Mater.* **5** 9–15
[42] Karamooz Ravari M, Kadkhodaei M and Ghaei A 2015 *J. Mater. Eng. Perform.* **24** 4096–105
[43] Karamooz Ravari M R, Kadkhodaei M and Ghaei A 2015 *J. Intell. Mater. Syst. Struct.* doi:10.1177/1045389X15604232
[44] Machado G, Louche H, Alonso T and Favier D 2015 *Mater. Des.* **65** 212–20
[45] Rahmanian R, Andani M T, Walker J, Habeland C, Elahinia M, Dean D and Miller M 2014 *ASME 2014 Conference on Smart Materials, Adaptive Structures and Intelligent Systems* vol 1 pp V001T03A032

[46] Rahmanian R, Moghaddam N S, Haberland C, Dean D, Miller M and Elahinia M 2014 *Proc. SPIE* **9058** 905814
[47] Walker J M 2014 Additive manufacturing towards the realization of porous and stiffness-tailored NiTi implants *PhD Thesis*
[48] Andani M T, Haberland C, Walker J and Elahinia M 2014 *ASME 2014 Conference on Smart Materials, Adaptive Structures and Intelligent Systems* vol 1 pp V001T01A026
[49] Meier H and Haberland C 2008 *Mater.Wiss. Werkst.Tech.* **39** 665–70
[50] Kadkhodaei M, Salimi M, Rajapakse R and Mahzoon M 2007 *Phys. Scr.* **T 129** 329 (2007)
[51] Kadkhodaei M, Salimi M H, Rajapakse R and Mahzoon M 2007 *J. Intell. Mater. Syst. Struct.* **19** 541–50
[52] Mehrabi R and Kadkhodaei M 2013 *Smart Mater. Struct.* **22** 025017
[53] Mehrabi R, Kadkhodaei M, Andani M T and Elahinia M 2014 *J. Intell. Mater. Syst. Struct.* **26** 144–55
[54] Mehrabi R, Kadkhodaei M and Elahinia M 2014 *Int. J. Solids Struct.* **51** 2666–75
[55] Mehrabi R, Kadkhodaei M and Elahinia M 2014 *Smart Mater. Struct.* **23** 75021–35
[56] Karamooz Ravari M, Kadkhodaei M and Ghaei A 2015 *Smart Mater. Struct.* **24** 075016
[57] Poorasadion S, Arghavani J, Naghdabadi R and Sohrabpour S 2013 *J. Intell. Mater. Syst. Struct.* **25** 1905–20
[58] ALTENBACH H and ÖCHSNER A 2010 *Cellular and Porous Materials in Structures and Processes* (NewYork: Springer)
[59] Bouvet C, Calloch S and Lexcellent C 2004 *European J. Mechanics-A/Solids* **23** 37–61
[60] Lubliner J and Auricchio F 1996 *Int. J. Solids Struct.* **33** 991–1003